
Prediction with directed transitions: complex eigenstructure, grid cells and phase coding

Changmin Yu
UCL
changmin.yu.19@ucl.ac.uk

Timothy E.J. Behrens
University of Oxford; UCL
behrens@fmrib.ox.ac.uk

Neil Burgess
UCL
n.burgess@ucl.ac.uk

Abstract

Markovian tasks can be characterised by a state space and a transition matrix. In mammals, the firing of populations of place or grid cells in the hippocampal formation are thought to represent the probability distribution over state space. Grid firing patterns are suggested to be eigenvectors of a transition matrix reflecting diffusion across states, allowing simple prediction of future state distributions, by replacing matrix multiplication with elementwise multiplication by eigenvalues. Here we extend this analysis to any translation-invariant directed transition structure (displacement and diffusion), showing that a single set of eigenvectors supports prediction via displacement-specific eigenvalues. This unifies the prediction framework with traditional models of grid cells firing driven by self-motion to perform path integration. We show that the complex eigenstructure of directed transitions corresponds to the Discrete Fourier Transform, the eigenvalues encode displacement via the Fourier Shift Theorem, and the Fourier components are analogous to "velocity-controlled oscillators" in oscillatory interference models. The resulting model supports computationally efficient prediction with directed transitions in spatial and non-spatial tasks and provides an explanation for theta phase precession and path integration in grid cell firing. We also discuss the efficient generalisation of our approach to deal with local changes in transition structure and its contribution to behavioural policy via a "sense of direction" corresponding to prediction of the effects of fixed ratios of actions.

1 Introduction

A "cognitive map" encodes relations between objects and supports flexible planning [33], with hippocampal place cells and entorhinal cortical grid cells thought to instantiate such a map [26; 18]. Each place cell fires when the animal is near a specific location, whereas each grid cell fires periodically when the animal enters a number of locations arranged in a triangular grid across the environment. Together, this system could support representation and flexible planning in state spaces where common representational structure is preserved across states and tasks, affording generalisation and inference, e.g., in spatial navigation where Euclidean transition rules are ubiquitous [36].

Recent work suggests that place cell firing provides a local representation of state occupancy, while grid cells comprise an eigenbasis of place cell firing covariance [14; 30; 29; 23]. Accordingly, grid cell firing patterns could be learned as eigenvectors of a symmetric (diffusive) transition matrix over state space, providing a basis set enabling prediction of occupancy distributions over future states. This "intuitive planning" operates by replacing multiplication of state representations by the transition matrix with multiplication of each basis vector by the corresponding eigenvalue [2; 12]. Thus a distribution over state space represented as a weighted sum of eigenvectors can be updated by re-weighting each eigenvector by its eigenvalue to predict future state occupancy.

While promising in its elegance and generality, the view of grid cell firing patterns as formed from place cell inputs is hard to reconcile with the traditional view of self-motion in updating grid cell firing (or "path integration"). In this view, directed actions have specific effects on state occupancy. In continuous attractor models this updating occurs via action-specific asymmetric connectivity [37; 17; 4], or by learned action-specific connections in deep variational encoders [36]. The oscillatory interference (OI) model, originally proposed to explain phase "precession" of place cells firing relative to the "theta" oscillation in runs through firing fields ("theta phase precession") [27], suggests that grid cell firing results from coincidence detection of velocity-controlled oscillators whose firing phases encode displacements along different axes [6; 35; 20].

Here we propose a generalised framework which seek to unify the prediction/intuitive planning and path integration views of grid cells, as well as generalising planning with grid codes to directed transition structure. Vector-based navigation using grid codes outperforms traditional reinforcement learning (RL) in spatial navigation tasks [1], and deeper understanding of grid codes could improve deep learning algorithms for navigation and planning. The immediate challenges are that directed transition matrices yield complex eigenstructure, and that transition dynamics associated with different actions will have different eigenbases. Accordingly we consider the set of Markovian, translation invariant transition matrices corresponding to diffusion and arbitrary drift velocities under periodic boundary conditions. We demonstrate flexible prediction using a single universal set of Fourier modes as eigenvectors. The relationship between the desired one-step translation and the complex phase of the eigenvalues is derived via the Fourier shift theorem [3]. Our formulation predicts the effects of actions (i.e. performs path integration) in a way analogous to OI models [7; 6], synthesises arbitrary distributions over the state space [35], and can implement "intuitive planning" under transitions including arbitrary translation.

2 "Intuitive planning" with symmetrical transitions

Intuitive planning represents distribution over the state space in terms of a weighted sum of the (real) eigenvectors of the (symmetric) transition matrix, so that the effect of one step of the transition dynamics on the distribution can be predicted by reweighting each of the eigenvectors by the corresponding eigenvalue, and that this generalises to calculating the cumulative effect of discounted future transitions [2].

Specifically, consider a transition matrix, $T \in \mathbb{R}^{N \times N}$, $T_{ss'} = \mathbb{P}(s_{t+1} = s' | s_t = s)$ where s_t encodes the state at time t and N is the number of states. Then, T^n is the n -step transition matrix, and has the same set of eigenvectors as T . Specifically, the eigendecomposition of T and T^n are:

$$T = Q\Lambda Q^{-1}, \quad T^n = Q\Lambda^n Q^{-1} \quad (1)$$

where each column of the matrix Q is an eigenvector of T and $\Lambda = \text{diag}(\sigma_P(T))$, where $\sigma_P(T)$ is the set of eigenvalues of T . Similarly any polynomial in T , $p(T)$, shares the same set of eigenvectors as T and the set of eigenvalues $\sigma_P(p(T)) = p(\sigma_P(T))$. Hence:

$$\sum_{k=0}^{\infty} (\gamma T)^k = (I - \gamma T)^{-1} = Q \text{diag}(\mathbf{w}) Q^{-1}, \quad \text{where } \mathbf{w} = \left\{ \frac{1}{1 - \gamma \lambda}, \text{ for } \lambda \in \sigma_P(T) \right\} \quad (2)$$

and the resolvent form in eq. 2 acts as distance metric between states in terms of future state occupancy (Fig. 1A-D) and can be interpreted as an infinite discounted sum of the transition matrix, or the successor representation in RL (SR, Fig. 1E) with discounting factor γ [13; 30]. The SR can be used for navigation via gradient ascent of the future probability of occupying the target state [2].

The eigenvectors of the diffusion transition matrix generally show grid-like patterns, suggesting a relationship to grid cells. However, intuitive planning cannot predict the effects of directed actions or drift (i.e., asymmetric transition structure), and thus understand how grid cell dynamics relate to directed actions and hence path integration. Moreover, it is inefficient to perform eigendecomposition separately for different actions. In Section 3 we unify the prediction and path integration approaches by exploiting translation invariant symmetries to generalise across actions, using a single common eigenbasis and cheap action-dependent eigenvalue updates.

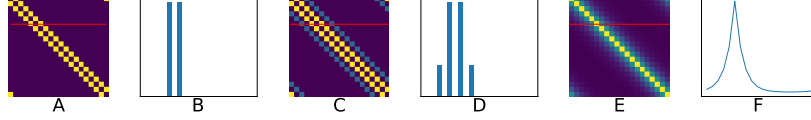


Figure 1: **Demonstration of intuitive planning on a diffusive transition task on a ring track with 20 states.** **Left panel:** **A:** T ; **B:** a slice through state 5 from T projected onto the state space, $\mathbb{P}(s_{t+1} = s' | s_t = 5)$; **C:** T^3 ; **D:** $\mathbb{P}(s_{t+3} = s' | s_t = 5)$; **E** Resolvent form (eq. 2; computed from locally-learned eigenstructures); **F** Discounted future state occupancy.

3 Flexible planning with directed transitions

Updating state representations to predict the consequences of arbitrary directed actions is an important ability of mobile animals, known as path integration [25]. To generalise to directed transition structures, we consider the translation invariant transition dynamics corresponding to translation (drift) and Gaussian diffusion with periodic boundary conditions. In this case the transition matrix is circulant and its eigenvectors form a basis set over the state space consists of Fourier modes. Hence representing the distribution over states (i.e. finding the coefficients for the weighted sum of Fourier components) is given by the discrete Fourier transform (DFT) of the distribution [3], and the eigenvalues are such that their magnitudes cause diffusion of the distribution and their complex phases cause translation, by shifting the phase of each Fourier component corresponding to the one-step translation relative to their wavevectors (as given by the Fourier shift theorem, or DFT of any row of the transition matrix). Importantly, the same set of Fourier components act as the eigenbasis for transition matrices corresponding to all possible translations, and therefore support prediction under arbitrary translation (or plain diffusion), via different sets of eigenvalues.

Consider a 2D rectangular environment with length L and width W where each state is a node of the unit square grid, then the transition matrix can be represented by $\mathbf{T} \in \mathbb{R}^{LW \times LW}$, with each row the vectorisation of the matrix of transition probabilities starting from the specified location, i.e., $\mathbf{T}[i, :] = \text{vec}[\mathbb{P}(s(t+1) | s(t) = i)]$, and \mathbf{T} is constructed by considering the 2D state space as a 1D vector and concatenating the rows ($i = xL + y$ for $(x, y) \in [0, W-1] \times [0, L-1]$), see Fig. 2A.

The transition matrix is circulant due to the translation invariance of the transition structure (see Appendix Prop. A.1), and takes the following form:

$$\mathbf{T} = \begin{bmatrix} T_0 & T_{LW-1} & \cdots & T_2 & T_1 \\ T_1 & T_0 & T_{LW-1} & \cdots & T_2 \\ \vdots & T_1 & T_0 & \ddots & \vdots \\ T_{LW-2} & \cdots & \ddots & \ddots & T_{LW-1} \\ T_{LW-1} & T_{LW-2} & \cdots & T_1 & T_0 \end{bmatrix} \quad (3)$$

The normalised eigenvectors of the circulant matrix $\mathbf{T} \in \mathbb{R}^{N \times N}$ ($N = LW$) are the vectors of powers of N th roots of unity:

$$\mathbf{q}_k = \frac{1}{\sqrt{N}} [1, \omega_k, \omega_k^2, \dots, \omega_k^{N-1}]^T \quad (4)$$

where $\omega_k = \exp(\frac{2\pi i}{N} k)$ is the k -th N -th root of unity, for $k = 0, \dots, N-1$, and $i = \sqrt{-1}$. Hence the matrix whose columns are the eigenvectors of the circulant matrix is:

$$F = (\mathbf{q}_0, \mathbf{q}_1, \dots, \mathbf{q}_{N-1}) \quad (5)$$

where $F_{kj} = \omega_j^k$ for $0 \leq k, j \leq N-1$. The Fourier modes projected back onto the $L \times W$ 2D spatial domain are plane waves, as shown in Fig. 2G, with wavevector determined by the value of k that specifies the direction and spatial frequency of each plane wave (see Appendix B). We could immediately compute the corresponding eigenvalues for the eigenvectors in eq. 5 (which is equivalent to taking the discrete Fourier transform (DFT) of the first row (or column) of T):

$$\lambda_m = \sum_{j=0}^{N-1} T_j \omega_j^m, \quad \text{for } m = 0, \dots, N-1 \quad (6)$$

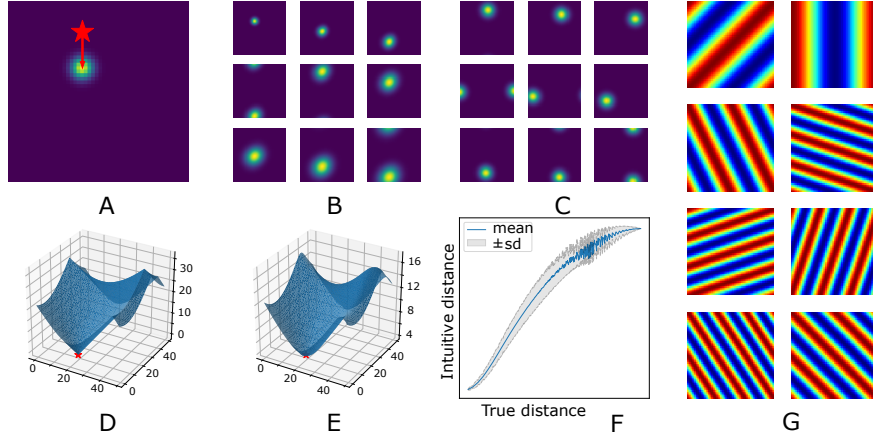


Figure 2: **Demonstration of our method in a 2D 50×50 environment with periodic boundary conditions.** **A:** Transition matrix $\mathbb{P}(x_{t+1} = (i', j') | x_t = (i, j))$ starting from a randomly chosen state $((8, 10))$; red star) with drift velocity 10 units southward and Gaussian diffusion (red arrow); **B:** Usage of the eigenbasis (eq. 5) and our analysis (eq. 9) for predicting the distribution over future states given the transition structure given in A, showing successive changes to state occupancy; **C:** Application of our model to translation-only transition structures (drift velocity $v = (3, 3)$); **(D-E):** Ground-truth shortest distance to state $(8, 20)$ (red star; D) as a function of starting location, and distance estimated as under the intuitive planning framework (E) using plain diffusion; **F:** Estimated distance measure (E) v.s. the corresponding ground-truth distance (D) over all pairs of states; **G:** Examples of 2D Fourier modes (real parts shown, see Appendix Fig. 7 for the top 100 eigenvectors).

where $\{T_0, \dots, T_{N-1}\}$ are the N unique elements that fully specifies the circulant matrix T (eq. 3). See Appendix Prop. A.2 for proof.

Now we have an efficient framework for determining the approximate eigenstructure of the transition matrix (eq. 5 and eq. 6). However, given that the agent’s velocity may change at every time point, in order to avoid recomputing the eigenvectors and eigenvalues for each new transition matrix we again utilise the circulant structure of all underlying transition matrices for cheap updating of the eigenvalues whilst requiring only one set of eigenvectors for all possible transitions.

For a transition matrix $\mathbf{T}^{\mathbf{v}}$ corresponding to an arbitrary action (translation velocity) $\mathbf{v} = (v_x, v_y)$, each row of $\mathbf{T}^{\mathbf{v}}$ is a circulant shifted version of the corresponding row vector of the symmetric transition matrix, \mathbf{T}^0 . Specifically, the first rows of the two matrices are related as follows:

$$\mathbf{T}^0(k + v_x L + v_y) = \mathbf{T}^{\mathbf{v}}(k), \quad \text{for } k = 0, \dots, N - 1 \quad (7)$$

Given the eigenvalues for \mathbf{T}^0 , $\Lambda^0 = [\lambda_0^0, \lambda_1^0, \dots, \lambda_{N-1}^0] \in \mathbb{C}^N$ (via the DFT of the first row of \mathbf{T}^0 , eq. 6). We can immediately derive the eigenvalues of $\mathbf{T}^{\mathbf{v}}$, $\Lambda^{\mathbf{v}}$, via the Fourier shift theorem [3] as:

$$\Lambda^{\mathbf{v}}[k] = \exp\left(-\frac{2\pi i}{N}(v_x L + v_y)k\right) \Lambda^0[k] \quad \text{for } k = 0, \dots, N - 1 \quad \text{for arbitrary } \mathbf{v} \quad (8)$$

$$\text{i.e., } \Lambda^{\mathbf{v}} = \Phi_{\delta(\mathbf{v})} \Lambda^0, \quad \Phi_{\delta(\mathbf{v})} = [1, \omega_{\delta(\mathbf{v})}, \omega_{\delta(\mathbf{v})}^2, \dots, \omega_{\delta(\mathbf{v})}^{N-1}], \quad \text{where } \delta(\mathbf{v}) = v_x L + v_y \quad (9)$$

Hence given the eigenvalues $\Lambda^0 \in \mathbb{C}^N$ for the diffusion transition matrix, we can compute the eigenvalues for diffusion plus an arbitrary translation velocity $v = (v_x(t), v_y(t))$, $\Lambda^{\mathbf{v}} \in \mathbb{C}^N$, via a one-step update without recomputing the eigendecomposition. This allows path integration by reweighting the common set of eigenvectors at each timestep by the eigenvalues corresponding to the current drift velocity (eq. 9; additionally reweighting by the eigenvalues of the diffusion transition matrix also allows tracking of increasing uncertainty). Our approach follows the Fourier shift theorem, where the Fourier components are eigenvectors of a transition matrix that includes translation [3], and the convolution theorem in replacing convolution of state representations and (circulant) transition matrices with the product of their Fourier transforms.

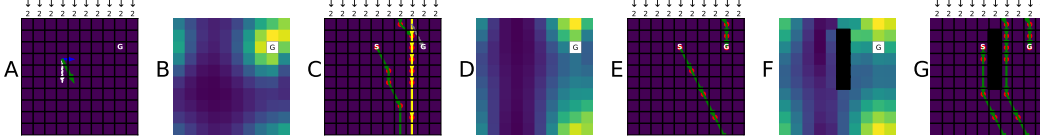


Figure 3: **Application to spatial navigation in a windy grid world.** **A:** The 10×10 windy grid world task environment (target state $(2, 8)$), with toroidal boundary conditions and a constant external force causing two units of displacement southward acting on every state (white arrow: wind; blue arrow: one-step action rightward; green arrow: resulting displacement); **B:** SR computed from symmetric diffusive transition matrix (without taking into account the wind); **C:** Path from the start state $(2, 4)$ to the target state following the diffusive SR (red dots are intermediate states, green arrows are one-step translations, yellow arrows are the repeated path, gray arrow indicates a path to the target state given a ϵ -greedy policy based on diffusive SR). **D:** SR under diffusion plus the wind effect; **E:** Path following the diffusion SR plus the wind effect; **F:** Updated diffusion SR plus wind given the insertion of a barrier (dark blocks); **G:** Path following the updated SR.

Utilising the fixed eigenbasis (eq. 5) and the respective eigenvalues (eq. 9) for arbitrary transition structures, we can predict the distribution of future state occupancy with respect to any action (see Figs. 2B-C). Indeed the discounted future occupancy of one state from another (eq. 2) closely matches the Euclidean distances between them (Figs. 2D-F).

Adding translation to the translation-invariant transition matrix does not change the set of eigenvectors - allowing one set of eigenvectors (Fourier modes) to support prediction for actions in all directions (or plain diffusion), and hence planning. The ability to do flexible planning under arbitrary drift velocity is demonstrated in Fig. 3, where we applied our model for planning in a windy grid world. We could try to navigate to a target state based on the SR (the resolvent metric, eq. 2) computed given plain diffusion without considering the wind (Fig. 3B). However, the ϵ -greedy policy following this diffusion SR takes circuitous path (Fig. 3C) by not taking the wind into account. By contrast, the policy following the SR computed from the (asymmetric) transition matrix including the effects of diffusion and wind (Fig. 3E) goes straight to the target (Fig. 3D), correctly adjusting for the wind.

Our approach is restricted to translation invariant transition structures hence cannot cope with state spaces with, e.g., a barrier in the middle (Fig. 3F). One way of generalising to such transition structures is to use a translation invariant SR to generate a default policy (see Section 4) from which an optimal value function could be learnt via reinforcement learning [31]. Here we demonstrate a more efficient approach, by directly updating the translation-invariant SR under diffusion and wind using the Woodbury matrix inversion formula (see Appendix Prop. A.3 and [28]). The updated SR given insertion of the barrier (Fig. 3F) captures the local changes in transition structure, and correctly navigates to the target state avoiding the barrier under the wind (Fig. 3G). However the path in Fig. 3G is suboptimal, which is possibly due to the fact that SRs do not account for the reward distribution, which could be alleviated by the linear RL approach in Section 4. Note that the other main limitation, the need for the toroidal boundary conditions, need not affect tasks implemented on subsections of state space much smaller than the torus.

4 "Sense of direction" based on grid cells

The SRs calculated in Section 3 (via eq. 2) under diffusion and any constant displacement (e.g., wind) can be used for navigation via a policy of gradient ascent in the discounted future probability of occupying the goal (Fig. 3). However, they do not offer directional or long-range policy information. Here we address this by calculating a set of SRs, each corresponding to repeated application of a specific action plus diffusion (similar to the SR corresponding to drift and diffusion, Fig. 3D). We can immediately compute the SRs given the different one-step actions (one unit to the N, S, E, W) in addition to diffusion and the wind effect, utilising our previous analysis (eq. 5, eq. 9; Fig. 4A). Then by "greedily" combining the action-specific SRs, we can compute a heuristic "greedy" SR (Fig. 4B), i.e., for each starting state, taking the discounted future occupancy of other states from the action-specific SRs with maximal occupancy of the goal state. This heuristic "greedy" SR corresponds to using a "sense of direction" for the goal, equivalent to a policy of taking the action

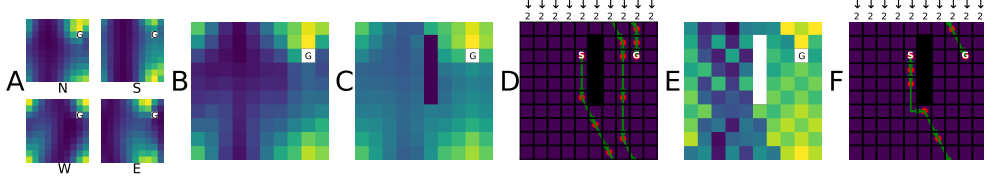


Figure 4: **Demonstration of a "sense of direction"**. **A**: Action-specific SRs corresponding to one-unit translations (N S E W) with diffusion and wind effect; **B**: Heuristic "greedy" combination of action-specific SRs; **C**: Updated "greedy" SR given insertion of the barrier; **D**: Path following the updated "greedy" SR; **E**: Optimal value function (v^*) computed via linear RL using the "greedy" SR for the default policy; **F**: Path following v^* .

that, if repeated in an uncluttered environment, would best lead to the goal. We can also update each action-specific SR given local changes in the transition structure as we did for the diffusion SR in Section 3, so we could estimate the updated pseudo "greedy" SR given the insertion of a barrier, by greedily combining the updated action-specific SRs. The paths following the updated pseudo SR yield similar paths to following the updated diffusive SR (Fig. 4D, Fig. 3G) but each state is directly related to an action (rather than having to use gradient ascent on the diffusion SR). Thus, navigation with the "greedy" SR, or "sense of direction" policy and is able to perform at least as well as the diffusion SR. See Appendix B for examples of the "sense of direction" policy improves navigation performance.

We could compute the SRs for translations in any directions for a goal state in addition to the NSEW translations. Hence a "sense of direction" (direction which most probably leads to the target state given a start state) can be derived by finding the direction, θ^* that maximises the discounted future occupancy of the goal state, i.e., using eqs. 2 and 9:

$$\theta^* = \arg \max_{\theta} \sum_j \frac{\exp[2\pi i(\mathbf{s}_G - \mathbf{s}_0) \cdot \mathbf{k}_j]}{1 - \gamma D_j \exp[2\pi i \mathbf{v}_{\theta} \cdot \mathbf{k}_j]} \quad (10)$$

where γ is the discounting factor, $D_j, j = 1, \dots, LW$ are the eigenvalues for the symmetric diffusion transition matrix, $\mathbf{k}_j, j = 1, \dots, LW$ are the wavevectors for the Fourier components, $\mathbf{s}_0, \mathbf{s}_G$ are the coordinates of the start and goal states, and $\mathbf{v}_{\theta} = (v \cos(\theta), v \sin(\theta))$ represents the velocity (with speed v and head direction θ). Note that the quantity in eq. 10, which is equivalent to the $[\mathbf{s}_0, \mathbf{s}_G]$ entry of the SR matrix, is real (due to the conjugacy of the eigenbasis regardless of \mathbf{v}), and that maximising eq. 10 implies that \mathbf{v}_{θ^*} aligns with the displacement between start and target states. We think grid cells may provide a sense of direction, exploiting translation invariant symmetries to indicate the best fixed ratio of actions irrespective of the details of the current environment, with other mechanisms refining policy, e.g., by adding obstacle avoidance [15]. See Appendix B for the derivation of eq. 10 and more details on "sense of direction".

In the presence of barriers (breaking the translation-invariance), the path following the updated "greedy" SR is not optimal. We could further improve navigation by taking the greedy SR as a default policy in linear RL to compute and update an approximate optimal value function (v^*) given local changes in the transition structure [32; 28] (see Appendix Prop. B.2). The resulting v^* clearly accommodates the insertion of the barrier (white blocks, Fig. 4E) and the policy given v^* yields more direct and shorter path comparing to the paths following the diffusive or "greedy" SR (Fig. 3G, Fig. 4F). Despite the apparent roughness observed in v^* (Fig. 4E), the resulting optimal value function is smooth given the effect of the wind and insertion of the barrier.

5 Relation to oscillatory interference models of path integration by grid cells

In oscillatory interference models, path integration is achieved by velocity controlled oscillators (VCOs), which encode movement speed and direction by variations in burst firing frequency [7; 6]. The VCOs generates grid-like firing patterns via coincidence detection by the grid cells [20; 35]. The variation of frequency with velocity produces a phase code for displacement, enabling the modelled grid cells to perform path integration, their often-supposed function [25; 4]. Namely, VCOs change their frequencies relative to the baseline according to the projection of current velocity, $v(t)$, onto the

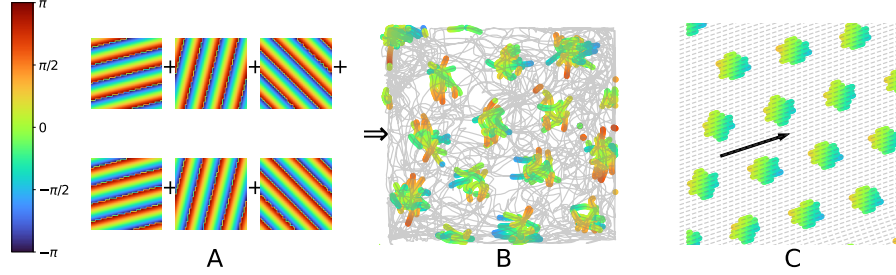


Figure 5: **Generated grid-like patterns given our model.** **A:** 6 input Fourier modes with the same wavelength (complex phases shown); **B:** Simulated grid cell firing given a real rat trajectory (gray line) using coincidence detection and baseline modulation given the 6 Fourier modes inputs in A, each spike is represented by a colored scatter with the color indicates the corresponding "theta" phase at the spiking time; **C:** Simulated grid cell firing fields given multiple runs in the same direction (black arrow) showing theta phase precession.

VCO's "preferred direction", \mathbf{d} :

$$f_a(t) = f_b(t) + \beta \mathbf{v}(t) \cdot \mathbf{d} \quad (11)$$

where β is a positive constant, and $f_b(t)$ is the baseline frequency (the 4 – 11Hz EEG theta rhythm). It follows that the VCOs perform linear path integration since the relative phase between VCO's frequency and baseline at time t , $\phi_{ab}(t) = \phi_a(t) - \phi_b(t)$, is proportional to the agent's displacement in the preferred direction:

$$\phi_{ab}(t) - \phi_{ab}(0) = \int_0^t 2\pi[f_a(\tau) - f_b(\tau)]d\tau = 2\pi\beta[\mathbf{x}_t - \mathbf{x}_0] \cdot \mathbf{d} \quad (12)$$

where $\mathbf{x}(t)$ is the agent's location at time t . The interference of VCOs whose preferred directions differ by multiples of $\pi/3$ generate triangular grid-like patterns, provides an explanation of theta phase precession in grid cells [19; 6] and complements the attractor dynamics given by symmetrical connections between grid cells [8].

Here we used the Fourier modes of the approximated circulant transition matrix, which take the form of plane waves with different directions and wavelengths (see supplementary Fig. 7). Since the set of Fourier modes comprises a basis for the state space, either a linearly weighted sum of Fourier modes, or coincidence detection of Fourier modes with specific wavevectors as in the OI model, can reproduce the triangular grid firing patterns (Fig. 5). In Supplementary Fig. 10 we show that the Fourier basis vectors can be used to synthesise arbitrary distributions over state space, e.g., corresponding to place cells [35]. The OI model and our scheme perform path integration or prediction in the same way. The OI model changes the phase of each VCO relative to baseline corresponding to the component of translation along the VCO's preferred direction. This is exactly analogous to multiplying the Fourier mode by its eigenvalue: shifting its complex phase corresponding to the component of translation along its wavevector (eq. 9).

In Fig. 5B we simulated the firing of a grid cell with the 6 Fourier modes as inputs, each firing a spike at its complex phase in the current state (Fig. 5A), as a leaky integrate and fire neuron performing coincidence detection using trajectory of a rat exploring a 50×50 box. At each time step (corresponding to one theta cycle), the phase of each Fourier mode is updated according to eq. 9 given the current velocity, and fires a spike at this phase if it is within the interval $[-\pi/4, \pi/4]$ (modelling modulation by the baseline theta oscillation). The grid cell fires a spike at the current location if the integrated inputs reach a threshold. We simulated one grid cell using the given Fourier modes, but we could simulate grid cells, with different offsets (depending on the initial phases of the Fourier modes) and different scales and orientations (depending on the choice of Fourier modes), such that the set of grid cells comprise a basis for the state space and do so on the basis of path integration (for which environmental inputs are also required to prevent error accumulation [6; 5]).

Grid cells show "precession" in their firing phase relative to theta as the animal moves through the firing field (signalling distance travelled within the field) [19; 21; 11], which can be captures by our

model, following the OI model [6]. The Fourier modes whose wavevectors are aligned with the current direction of translation advance in phase as the movement progresses. Phase precession results from assuming that the Fourier modes aligned with movement direction are dominant influence on grid cell firing (c.f. those aligned to the reverse direction). The baseline "theta frequency" corresponds to the mean rate of change of phase of all Fourier components and so could vary (to reduce noise [5; 6], without precluding phase coding [16; 9]). By simulating random straight runs, we can see clear late-to-early phase precession.

6 Discussion

Representing state occupancy distributions as a weighted sum of eigenvectors of the transition matrix facilitates prediction of future state occupancy, replacing multiplication by the transition matrix by reweighting the eigenvectors with their corresponding eigenvalues. This is useful for planning, and grid cell firing patterns have been proposed to be the eigenvectors of a diffusive transition matrix (or the covariance of the firing of place cells representing states). However, this approach does not apply to (asymmetric) directed transition and makes no contact with evidence that grid cells are driven by actions to update state occupancy (path integration).

Here we unify prediction and path integration approaches, by exploiting translation invariant symmetries to find a single common eigenbasis (Fourier modes) that generalises prediction across actions via translation-specific (complex) eigenvalues. This corresponds directly to models of path integration, in which displacement is encoded by the phase of firing relative to the theta rhythm (represented here by the complex phases being updated via multiplication by complex eigenvalues). The Fourier modes can be combined as grids to facilitate noise cancellation [5], and association with states (i.e., providing distinct peaks for Hebbian association with specific states represented by place cells). This model is computationally efficient (avoids expensive operations, e.g., inverting large transition matrices, or computing the eigendecomposition), and provides cheap "sense of direction" planning (i.e. predicting the effect of repeating a fixed ratio of actions irrespective of environmental obstacles). Our approach generalises across tasks with similar translation invariant transition structures and to related non-spatial tasks such as transitive inference [34], we provide a self-contained trivial example in Appendix C.

The current model predicts future state occupancy from the transition matrix, but future work could look at the reverse: vector navigation, i.e., inferring the translation between two locations given the phase codes for each [10] (corresponding to discriminative and generative models). It might be that the grid cells/Fourier modes provide navigational direction, while other processes deal with obstacles [15; 24], or that direct translations occur in clear regions of state space between "bottlenecks" that are also identified by spectral methods [30].

In continuous attractor network (CAN) models of grid cell firing, path integration is achieved by pre-tuned asymmetrical weights, which play the role of the transition matrix to update the firing fields to reflect displacements [17; 4]. Further work could look at the possible equivalence between Fourier analysis of CANs and the spectral-based or VCO models and machine learning models to explain grid pattern formation and how grid cells encode structural information [36].

A key limitation of the current model is that it only applies to translation-invariant transition structures, and use of the Fourier shift theorem to calculate eigenvalues also assumes a Euclidean state space. However, we demonstrated one way of generalising planning to locally non-translation invariant transition structures by inserting a barrier in Section 3. We note that machine learning methods based on a similar premise (creating a single representation to support planning via multiple different actions) might work even when the transitions are not strictly translation invariant (e.g., family trees [36]). One way to generalise our model would be to try to apply a similar Fourier analysis to arbitrary set of transitions that form a compact group over the state space [22], as this is probably the minimal requirement to allow the type of powerful inference over the effects of actions employed here. This might enable application to domains far from physical space, including aspects of logical or linguistic processing.

Broader impact

We believe this work may be of benefit to scientists and engineers wanting to understand a) how to take advantage of translation invariance symmetries to make efficient predictions for planning, b) the functions of grid cells and theta phase precession, or c) the links between neural mechanisms for planning and path integration. More broadly speaking, this work may lead to more general and cheaper vector-based algorithms to aid reinforcement learning in spatial and non-spatial inference tasks. We do not believe there are specific ethical or societal risks associated with this research.

Acknowledgements

C.Y. thanks a DeepMind PhD studentship offered by the UCL Centre for Artificial Intelligence. T.E.J.B and N.B. thank the Wellcome Collaborative Award (214314/Z/18/Z) “Organising knowledge for flexible behaviour in the prefrontal hippocampal circuitry”. The authors would like to thank Daniel Bush, Talfan Evans, Kimberly Stachenfeld, Will de Cothi and Maneesh Sahani for helpful comments and discussions. The authors declare no competing financial interests.

References

- [1] A. Banino, C. Barry, B. Uria, C. Blundell, T. Lillicrap, P. Mirowski, A. Pritzel, M. J. Chadwick, T. Degris, J. Modayil, et al. Vector-based navigation using grid-like representations in artificial agents. *Nature*, 557(7705):429–433, 2018.
- [2] A. B. Baram, T. H. Muller, J. C. Whittington, and T. E. Behrens. Intuitive planning: global navigation through cognitive maps based on grid-like codes. *bioRxiv*, page 421461, 2018.
- [3] R. N. Bracewell. *The Fourier transform and its applications*, volume 31999. McGraw-Hill New York, 1986.
- [4] Y. Burak and I. R. Fiete. Accurate path integration in continuous attractor network models of grid cells. *PLoS computational biology*, 5(2), 2009.
- [5] C. P. Burgess and N. Burgess. Controlling phase noise in oscillatory interference models of grid cell firing. *Journal of Neuroscience*, 34(18):6224–6232, 2014.
- [6] N. Burgess. Grid cells and theta as oscillatory interference: theory and predictions. *Hippocampus*, 18(12):1157–1174, 2008.
- [7] N. Burgess, C. Barry, and J. O’keefe. An oscillatory interference model of grid cell firing. *Hippocampus*, 17(9):801–812, 2007.
- [8] D. Bush and N. Burgess. A hybrid oscillatory interference/continuous attractor network model of grid cell firing. *Journal of Neuroscience*, 34(14):5065–5079, 2014.
- [9] D. Bush and N. Burgess. Advantages and detection of phase coding in the absence of rhythmicity. *Hippocampus*, 2020.
- [10] D. Bush, C. Barry, D. Manson, and N. Burgess. Using grid cells for navigation. *Neuron*, 87(3): 507–520, 2015.
- [11] J. R. Climer, E. L. Newman, and H. M. E. Phase coding by grid cells in unconstrained environments: two-dimensional phase precession. *European Journal of Neuroscience*, 38(4): 2526–2541, 2013.
- [12] D. S. Corneil and W. Gerstner. Attractor network dynamics enable preplay and rapid path planning in maze-like environments. In *Advances in neural information processing systems*, pages 1684–1692, 2015.
- [13] P. Dayan. Improving generalization for temporal difference learning: The successor representation. *Neural Computation*, 5(4):613–624, 1993.

- [14] Y. Dordek, D. Soudry, R. Meir, and D. Derdikman. Extracting grid cell characteristics from place cell inputs using non-negative principal component analysis. *Elife*, 5:e10094, 2016.
- [15] V. Edvardsen, A. Bicanski, and N. Burgess. Navigating with grid and place cells in cluttered environments. *Hippocampus*, 2019.
- [16] T. Eliav, M. Geva-Sagiv, M. M. Yartsev, A. Finkelstein, A. Rubin, L. Las, and N. Ulanovsky. Nonoscillatory phase coding and synchronization in the bat hippocampal formation. *Cell*, 175(4):1119–1130, 2018.
- [17] M. C. Fuhs and D. S. Touretzky. A spin glass model of path integration in rat medial entorhinal cortex. *Journal of Neuroscience*, 26(16):4266–4276, 2006.
- [18] T. Hafting, M. Fyhn, S. Molden, M.-B. Moser, and E. I. Moser. Microstructure of a spatial map in the entorhinal cortex. *Nature*, 436(7052):801–806, 2005.
- [19] T. Hafting, M. Fyhn, T. Bonnevie, M.-B. Moser, and E. I. Moser. Hippocampus-independent phase precession in entorhinal grid cells. *Nature*, 453(7199):1248–1252, 2008.
- [20] M. E. Hasselmo. Grid cell mechanisms and function: contributions of entorhinal persistent spiking and phase resetting. *Hippocampus*, 18(12):1213–1229, 2008.
- [21] A. Jeewajee, C. Barry, V. Douchamps, D. Manson, C. Lever, and B. N. Theta phase precession of grid and place cell firing in open environments. *Philosophical Transactions of the Royal Society B: Biological Sciences*, 369(1635):20120532, 2014.
- [22] R. Kondor and S. Trivedi. On the generalization of equivariance and convolution in neural networks to the action of compact groups. *arXiv preprint arXiv:1802.03690*, 2018.
- [23] E. Kropff and A. Treves. The emergence of grid cells: Intelligent design or just adaptation? *Hippocampus*, 18(12):1256–1269, 2008.
- [24] E. A. Maguire, N. Burgess, J. G. Donnett, R. S. Frackowiak, C. D. Frith, and J. O’Keefe. Knowing where and getting there: a human navigation network. *Science*, 280(5365):921–924, 1998.
- [25] B. L. McNaughton, F. P. Battaglia, O. Jensen, E. I. Moser, and M.-B. Moser. Path integration and the neural basis of the ‘cognitive map’. *Nature Reviews Neuroscience*, 7(8):663–678, 2006.
- [26] J. O’Keefe and J. Dostrovsky. The hippocampus as a spatial map: preliminary evidence from unit activity in the freely-moving rat. *Brain research*, 1971.
- [27] J. O’Keefe and M. L. Recce. Phase relationship between hippocampal place units and the eeg theta rhythm. *Hippocampus*, 3(3):317–330, 1993.
- [28] P. Piray and N. D. Daw. A common model explaining flexible decision making, grid fields and cognitive control. *bioRxiv*, page 856849, 2019.
- [29] B. Sorscher, G. Mel, S. Ganguli, and S. Ocko. A unified theory for the origin of grid cells through the lens of pattern formation. In *Advances in Neural Information Processing Systems*, pages 10003–10013, 2019.
- [30] K. L. Stachenfeld, M. M. Botvinick, and S. J. Gershman. The hippocampus as a predictive map. *Nature neuroscience*, 20(11):1643, 2017.
- [31] R. S. Sutton and A. G. Barto. *Reinforcement learning: An introduction*. MIT press, 2018.
- [32] E. Todorov. Linearly-solvable markov decision problems. In *Advances in neural information processing systems*, pages 1369–1376, 2007.
- [33] E. C. Tolman. Cognitive maps in rats and men. *Psychological review*, 55(4):189, 1948.
- [34] L. Von Fersen, C. D. Wynne, J. D. Delius, and J. E. Staddon. Transitive inference formation in pigeons. *Journal of Experimental Psychology: Animal Behavior Processes*, 17(3):334, 1991.

- [35] A. C. Welday, I. G. Shlifer, M. L. Bloom, K. Zhang, and H. T. Blair. Cosine directional tuning of theta cell burst frequencies: evidence for spatial coding by oscillatory interference. *Journal of Neuroscience*, 31(45):16157–16176, 2011.
- [36] J. C. Whittington, T. H. Muller, S. Mark, G. Chen, C. Barry, N. Burgess, and T. E. Behrens. The tolman-eichenbaum machine: Unifying space and relational memory through generalisation in the hippocampal formation. *bioRxiv*, page 770495, 2019.
- [37] K. Zhang. Representation of spatial orientation by the intrinsic dynamics of the head-direction cell ensemble: a theory. *Journal of Neuroscience*, 16(6):2112–2126, 1996.

A Proofs in Sections 3

Proposition A.1 *Given our assumption of periodic boundary condition, the transition matrix, $T \in \mathbb{C}^{N \times N}$ (eq. 3), is indeed a circulant matrix.*

Proof It is easy to see that the proposition holds trivially for transition matrices with only one-step translations but without Gaussian spread. Hence here we only show the proof for the case where the transition structure includes both Gaussian spread and one-step translations.

Consider for an arbitrary transition matrix T for a 2D rectangular environment with length L and width W , and the underlying transition velocity is $v = (v_x, v_y)$, remembering that \mathbf{T} is the $LW \times LW$ 2D matrix formed from concatenating rows from what would be the 4D matrix of transitions between all pairs of states in a $L \times W$ 2D state space. An arbitrary entry on the k th lower subdiagonal is $T_{i, i-k} = \mathbb{P}(x(t+1) = i-k | x(t) = i)$ for any suitable state i given k (i.e., $i \geq k$). If the Gaussian spread is radially symmetric with constant variance across states, the value of $T_{i, i-k}$ only depends on the distance between state $i-k$ and the state i_v , where i_v is the translated state of state i given the effect of the velocity v . The states $i-k$ and i_v are equivalent to the states $((i-k)/L, (i-k) \bmod L)$ and $(i/L + v_x, i \bmod L + v_y)$ in the two-dimensional spatial domain respectively (where a/b denotes the integer part of a/b). Note that we need to have the velocity $v \in [\pm L/2, \pm W/2]$ so that the translation leaves the actual distance d unchanged. The distance between the state $i-k$ and the expected state i_v in the 2D state space is then

$$d = \sqrt{((i-k)/L - i/L - v_x)^2 + ((i-k) \bmod L - i \bmod L - v_y)^2} \quad (13)$$

For any arbitrary $i' \neq i$ such that $i' = i + m$, we could compute similarly the distance between state $i' - k$ and its corresponding expected state (Gaussian center) $i' + v$. After some algebra, we have that the distance between states $i-k$ and $i+v$ equals the distance between states $i' - k$ and $i' + v$.

$$\begin{aligned} d' &= \sqrt{((i'-k)/L - i'/L - v_x)^2 + ((i'-k) \bmod L - i' \bmod L - v_y)^2} \\ &= \sqrt{((i+\delta-k)/L - (i+\delta)/L - v_x)^2 + ((i+\delta-k) \bmod L - (i+\delta) \bmod L - v_y)^2} \end{aligned} \quad (14)$$

Now if we look at the two square terms within the square root separately, we have

$$\begin{aligned} &((i+\delta-k)/L - (i+\delta)/L - v_x)^2 \\ &= ((i-k)/L + \delta/L - i/L - \delta/L - v_x)^2 \\ &= ((i-k)/L - i/L - v_x)^2 \end{aligned} \quad (15)$$

$$\begin{aligned} &((i+\delta-k) \bmod L - (i+\delta) \bmod L - v_y)^2 \\ &= (((i-k) \bmod L + \delta \bmod L) \bmod L - (i \bmod L + \delta \bmod L) \bmod L - v_y)^2 \\ &= ((i-k) \bmod L + \delta \bmod L - i \bmod L - \delta \bmod L - v_y)^2 \\ &= ((i-k) \bmod L - i \bmod L - v_y)^2 \end{aligned} \quad (16)$$

The second equality holds due to the fact that $(i-k) \bmod L + \delta \bmod L \leq L$ since this is simply the x -position of state $i+\delta-k$, which is never larger than L , hence $((i-k) \bmod L + \delta \bmod L) \bmod L = (i-k) \bmod L + \delta \bmod L$. Similarly $(i \bmod L + \delta \bmod L) \bmod L = i \bmod L + \delta \bmod L$. Hence we have

$$d' = \sqrt{((i'-k)/L - i'/L - v_x)^2 + ((i'-k) \bmod L - i' \bmod L - v_y)^2} = d \quad (17)$$

Hence all entries on the k th lower subdiagonal are identical, i.e. $T_{i, i-k} = T_{i', i'-k}$ for all $1 \leq k \leq LW - 1$. And by similar arguments, we could show that all entries on the k th upper subdiagonal are identical (for $1 \leq k \leq LW - 1$), and equals to the corresponding entries on the $LW - k$ th lower subdiagonals. And the fact that all the main diagonal entries are identical is immediate from the problem setting. Hence our target transition matrix is indeed a circulant matrix. (Note that in simulations the transition matrix will only be approximately circulant due to normalisation and numerical issues.)

Now we consider the corresponding $(LW - k)$ th upper subdiagonal (to the k th lower subdiagonal), by similar arguments, we have that for any $T_{i'', i''+k} = \mathbb{P}(x(t+1) = i'' + k | x(t) = i'')$ for suitable i'' (i.e. $i'' + k \leq L$), the distance between the state $i'' + k$ and expected next state $i'' + v_t$ are the same as d , which is equivalent to $T_{i'', i''+k} = T_{i, k-i}$. Hence all entries on the $(LW - k)$ th upper subdiagonal are identical and equal to the entries on the k th lower subdiagonal. This holds for arbitrary $1 \leq k \leq LW - 1$. \square

Proposition A.2 For any circulant matrix $T \in \mathbb{C}^{N \times N}$ as shown in eq. 3, its k th eigenvector takes the form:

$$\mathbf{v}^k = \frac{1}{\sqrt{N}} [1, \omega_k, \omega_k^2, \dots, \omega_k^{N-1}]^T \quad (18)$$

where $\omega_k = \exp\left(\frac{2\pi ki}{N}\right)$ is the k th N th root of unity, and the set of eigenvalues equals to the set of DFTs of an arbitrary row/column of T .

Proof Firstly, note that the product between the circulant matrix T and an arbitrary vector \mathbf{v} is equivalent to a convolution.

$$\mathbf{w} = T \cdot \mathbf{v} = \begin{bmatrix} T_0 & T_{N-1} & \cdots & T_2 & T_1 \\ T_1 & T_0 & T_{N-1} & \cdots & T_2 \\ \vdots & T_1 & T_0 & \ddots & \vdots \\ T_{N-2} & \cdots & \ddots & \ddots & T_{N-1} \\ T_{N-1} & T_{N-2} & \cdots & T_1 & T_0 \end{bmatrix} \cdot \begin{bmatrix} v_0 \\ v_1 \\ \vdots \\ v_{N-1} \end{bmatrix} \quad (19)$$

And we immediately have that

$$w_k = \sum_{j=0}^{N-1} T_{j-k} v_j \quad (20)$$

This is true due to the periodicity of the entries given by the circulant structure. Then if we take the dot product of T and an arbitrary vector \mathbf{v}^m of the form shown in eq. 18, the l th entry of the output vector has the following form.

$$\sum_{j=0}^{N-1} T_{j-l} \omega_j^m = \omega_l^m \sum_{j=0}^{N-1} T_{j-l} \omega_{j-l}^m \quad (21)$$

where the equality holds since $\omega_j^m = \exp\left(\frac{2\pi i}{N} jm\right) = \exp\left(\frac{2\pi i}{N}(j-l)m\right) \exp\left(\frac{2\pi i}{N} lm\right) = \omega_l^m \omega_{j-l}^m$. Note that the last sum in Eq. 21 is independent of the choice of l since both T_j and ω_j are periodic hence any change in l is simply rearranging the terms in the summation. Also we have that $\omega_l^m = \omega_m^l$ is the l th entry of the eigenvector \mathbf{v}_m . Hence we have

$$T \mathbf{v}_m = \lambda_m \mathbf{v}_m \quad (22)$$

where

$$\lambda_m = \sum_{j=0}^{N-1} T_j \omega_j^m \quad (23)$$

for $m = 0, \dots, N - 1$. Hence for an arbitrary $N \times N$ circulant matrix T , the eigenvalues take the form as shown in eq. 23 and the corresponding eigenvectors take the form as shown in eq. 18, and the eigenvalues are equivalent to the DFT of the first row of the circulant matrix immediately follows from eq. 23 and the definition of DFT [3]. \square

The predicted phase change in the eigenvalues over the eigenvalues of the baseline symmetric transition matrix computed with Fourier modes computed via Fourier shift theorem (eq. 9) under our formulation perfectly captures the actual phase changes caused by the one-step translations in the eigenvalues between the symmetric and asymmetric transition matrices, as shown in Fig. 6A. However, when the transition dynamics is a combination of diffusion and one-step translations, the predicted phase changes in eigenvalues will no longer perfectly match the actual phase changes observed as shown in Fig. 6B, and the oscillation is caused by the diffusion process. Namely, although the expected translation is indicated by the velocity, the actual translation spans a range of states depending on the width of the diffusion field.

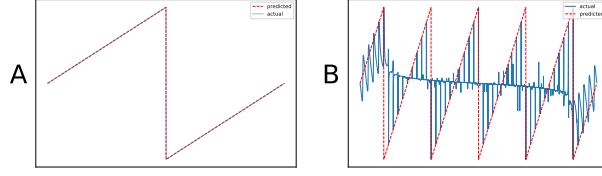


Figure 6: **Application of Fourier shift theorem for predicting changes in eigenvalues.** The blue lines and red dotted lines represent the actual and predicted shifts in complex phases of the eigenvalues of transition matrices given some drift velocity and the symmetric transition matrix where the transition dynamics are **A**: translation only (5 units rightward); **(B)**: diffusion with one-step translations (5 states rightward + diffusion).

Proposition A.3 *The updated SR given the insertion of a barrier, following Piray and Daw [28], is*

$$S = S_0 - C(I + RC)^{-1}RS_0 \quad (24)$$

where S_0 and S are the initial and updated SR, $R = S_0[J, :]$ and $C = S_0[:, J]$ are the J -th rows and columns of S_0 respectively, where J is the index set of states adjacent to the inserted barrier.

Proof Given the definition of the SR, we have

$$S = (I - \gamma T)^{-1}, \quad S_0 = (I - \gamma T_0)^{-1} \in \mathbf{R}^{N \times N} \quad (25)$$

where N is the number of states. Given the insertion of a barrier, S and S_0 only differ in their j -th rows for $j \in J$ where J is the index set of states adjacent to the barrier. Hence we could write:

$$R = T[J, :] - T_0[J, :] \in \mathbb{R}^{|J| \times N} \quad (26)$$

Then if we have $E \in \mathbb{R}^{|J| \times N}$ with zeros everywhere but ones on the j -th rows for $j \in J$, then by setting $W = I - T$ and $W_0 = I - T_0$, we could write:

$$W = W_0 + ER \quad (27)$$

Then by the Woodbury inversion formula, we have:

$$\begin{aligned} W^{-1} &= W_0^{-1} - EW_0^{-1} * (I + REW_0^{-1})^{-1}RW_0^{-1} \\ \Rightarrow S &= S_0 - C(I + RC)^{-1}RS_0 \end{aligned} \quad (28)$$

where $C = ES_0$ are the j -th columns of S_0 for $j \in J$. \square

B Correspondence with oscillatory interference models

We know that the Fourier basis vectors from eq. 5 form plane waves as shown in Fig. 5. From standard Fourier analysis in 2D space, the 2D Fourier modes form an orthonormal basis, and takes the following form.

$$\mathbf{v}_{\mathbf{u}}[\mathbf{x}] = \exp(2\pi i \mathbf{u} \cdot \mathbf{x}) \quad (29)$$

where the 2D Fourier basis vectors are encoded by the position vectors $\mathbf{u} = (u_1/L, u_2/W) \in [0, 1] \times [0, 1]$ (position vectors of each location in the $L \times W$ environment projected onto $[0, 1] \times [0, 1]$). The direction of the encoder position vector \mathbf{u} represents the direction of the plane wave and the frequency of the plane wave is the unnormalised direction vector $\|\mathbf{u}'\|$ (where $\mathbf{u}' = \mathbf{u} \times (L, W)$), note that \mathbf{u}' is also the wavevector for the plane wave. This is a slightly different formulation comparing to the formulation given in eq. 5, which consider the state space as a 1-dimensional flattened vector of the 2-dimensional environment, hence the Fourier basis vectors are the corresponding 1-dimensional Fourier modes. Though both formulation give us the same set of Fourier basis vectors, under the definition in eq. 29, we could easily track the frequency and direction of the plane wave formed from the 2D Fourier modes. And the phase shift via the Fourier shift theorem 9 equivalently applies for this 2D Fourier formulation. In Fig. 7 we show the phase plots of 100 low-frequency 2D Fourier basis vectors.

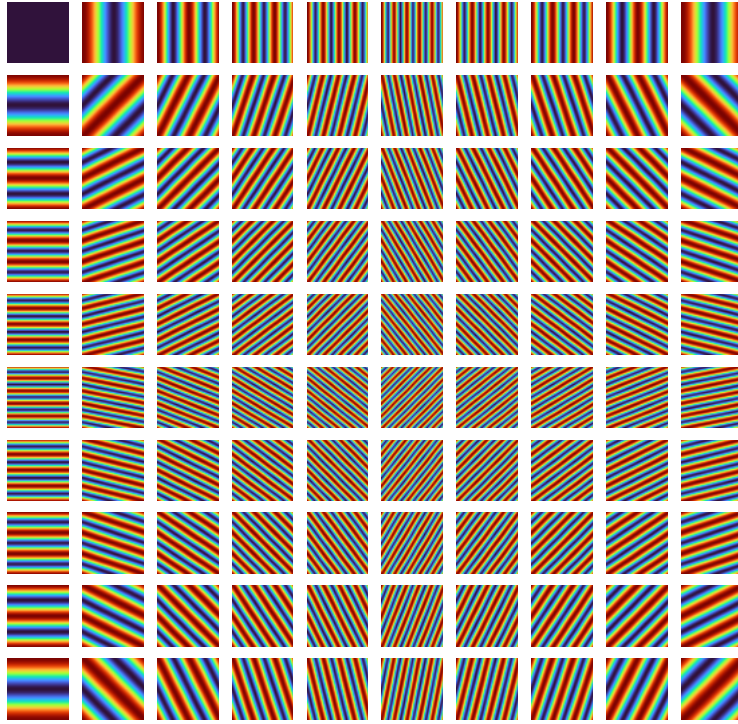


Figure 7: Phase plots of 100 chosen low-frequency Fourier basis vectors with different frequencies and wavevectors.

The grid-like firing patterns can be generated via coincidence detection of VCOs, and the Fourier modes are able to simulate grid cells under the same formulation. Moreover we could also generate grid cells with various spacings and orientations (Fig. 10B). Note that during movement, the firing of

the grid cells generated via both the OI models and the Fourier modes are dependent on the velocity and baseline modulation (i.e., VCOs or Fourier modes with preferred directions or wavevectors differing from the current heading direction by more than $\pi/2$, or with phases outside $[-\pi/4, \pi/4]$, are inhibited from firing, see Fig. 6). However, the two models differ in that the frequencies of VCOs are explicitly simulated and their phases are measured relative to a baseline oscillation taking the mean frequency of all VCOs [6] which allows noise cancellation [5], whereas the complex phase of the Fourier modes simply reflects the phase relative to this baseline. Note that the absence of a stable baseline frequency does not preclude phase coding [16; 9].

The Fourier modes comprises a basis for representing any distribution over the task state space, so we could use a linearly weighted combination of Fourier modes to reconstruct any firing patterns, such as those observed in place cells [35] (Fig. 10). However note that the coincidence detection of small numbers of oscillators with different frequencies will generate periodic patterns, e.g., grid cells, and more oscillators will be needed for those with more local firing fields such as place cells. Note that the total number of Fourier modes equals the number of states in the environment (e.g., LW for the $L \times W$ rectangular environment on a square grid), and it could be infeasible and inefficient to compute and store a large number of such Fourier modes (or neurons with VCO-like firing patterns) in the brain. Hence here we only use the principal modes (taking the top n Fourier basis vectors in terms of the corresponding eigenvalues (frequencies)). This is valid since for any pattern we wish to reconstruct, the majority of the information is contained within the Fourier basis vectors with lower frequencies, with n depending on the desired reconstruction resolution. We only use a small set of the Fourier modes based on their eigenvalues with respect to the specific task structure as the basis vectors for doing planning and generating firing patterns (or alternatively we could maintain a fixed small set (100) of low-frequency Fourier basis vectors, see Fig. 7 for a typical fixed set of Fourier modes). Fig. 10 demonstrates that the small number of Fourier modes are able to reconstruct grid cells firing fields with various spacings and orientations, and place cells firing fields.

Proposition B.1 *The "sense of direction", θ^* , can be computed via maximising eq. 10.*

Proof Essentially, we wish to find value of θ such that under the drift velocity $\mathbf{v}_\theta = (v \cos(\theta), v \sin(\theta))$, given the start and target states, \mathbf{s}_0 and \mathbf{s}_G , the future discounted occupancy of \mathbf{s}_G starting from \mathbf{s}_0 (or $W[\mathbf{s}_0, \mathbf{s}_G]$, where W is the SR matrix), is maximised. Under our formulation, W can be calculated as follows:

$$W = F \text{diag}(1/(1 - \gamma \Lambda^{\mathbf{v}_\theta})) F^{-1} \quad (30)$$

where F is the DFT matrix (eq. 5), and $\Lambda^{\mathbf{v}_\theta}$ is the set of eigenvalues of the transition matrix given velocity \mathbf{v}_θ . From our analysis based on Fourier shift theorem (eq. 9), for each $\lambda_i^{\mathbf{v}_\theta} \in \Lambda^{\mathbf{v}_\theta}$, we have that:

$$\lambda_i^{\mathbf{v}_\theta} = D_i \omega^{\mathbf{v}_\theta \cdot \mathbf{k}_i} \quad (31)$$

where D_i is the i th eigenvalue of the symmetric (baseline) diffusion transition matrix, and \mathbf{k}_i is the wavevector for the i th Fourier mode. Then using linear algebra, we immediately arrive at the expression in eq. 10. \square

Note that in Section 4 we stated that the path following the updated heuristic "greedy" SR is at least as good as the updated diffusive SR. In Fig. 8 we see that in some cases, the implicit "sense of direction" implied by the heuristic "greedy" SR indeed finds a shorter path than the plain diffusive SR given the same pair of start and target states.

Moreover, the optimal value function computed given the default policy as the "sense of direction" policy (v_{sense}^* ; Section. 4; Fig. 9A) show significant improvement over that computed with the default policy computed from the diffusion SR ($v_{\text{diffusion}}^*$; Fig. 9C). Clearly the path following v_{sense}^* directly navigates to the target state whereas the path following $v_{\text{diffusion}}^*$ takes the opposite direction and results in a more circuitous path.

Proposition B.2 *[Following Todorov [32]] The optimal value function $\mathbf{v}^* \in \mathbb{R}^{LW-1}$ for all non-terminal states (assuming there is only one target, terminal state), is given by a linear equation:*

$$\exp(\mathbf{v}^*) = \mathbf{M} \mathbf{P} \exp(\mathbf{r}) \quad (32)$$

where $\mathbf{P} = \mathbf{T}_{NT}$ is the transition matrix between the non-terminal states and the target state, and \mathbf{M} is the "default representation" matrix:

$$\mathbf{M} = (\text{diag}(\exp(-\mathbf{r}_N/\lambda)) - \mathbf{T}_{NN})^{-1} \quad (33)$$

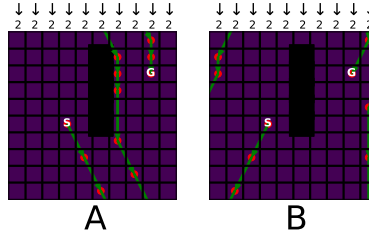


Figure 8: **Demonstration of heuristic "greedy" SR outperforming the diffusive SR.** **A:** Path following the updated diffusive SR (Fig. 3F, length: 11 steps); **B:** Path following the updated heuristic "greedy" SR (Fig. 4C, length: 9 steps).

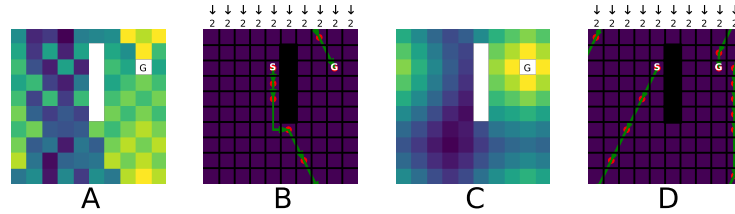


Figure 9: **Demonstration of "sense of direction" when combined with linear RL.** **A:** Optimal value function computed using linear RL given the "sense of direction" policy as default policy (v_{sense}^*); **B:** Path from the start state ((4, 2)) to the target state ((8, 2)) following v_{sense}^* ; **C:** Optimal value function given the default policy derived from the diffusion SR ($v_{\text{diffusion}}^*$); **D:** Path following $v_{\text{diffusion}}^*$.

where \mathbf{r}_N is the vector of rewards at non-terminal states, λ is a constant coefficient controlling the KL-divergence (between the default policy and the optimal policy) penalty, and \mathbf{T}_{NN} is the transition matrix between the non-terminal states.

Proof Please see Todorov [32] Section 2 for details of the derivation of eq. 32. □

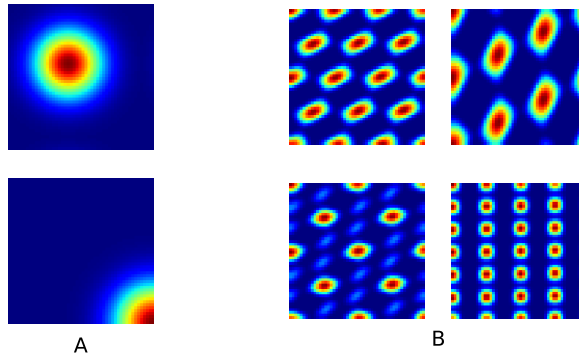


Figure 10: **Constructed place cell and grid cell firing fields from Fourier modes.** **A:** Place cells firing fields constructed from coincidence detection of selected input Fourier modes (bottom plot shows a place field restricted to a small subset of the toroidal state space); **B:** Grid cell firing fields with various spacings and orientations constructed from principal Fourier modes (Fig. 7).

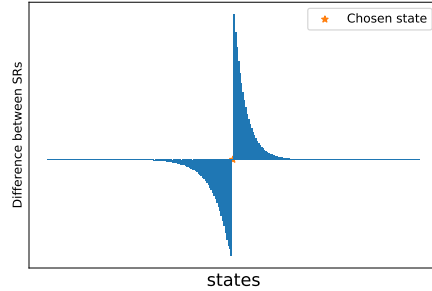


Figure 11: **Generalisation of flexible planning on transitive inference task.** Given $\{x_i\}_{i=0}^{259}$ such that $x_i > x_{i+1}$ for all i (and $x_{259} > x_0$ for ensuring the circulant structure). The bar plot shows that we can correctly infer transitive relations between the chosen state x_{129} (red star) and nearby target states via computing the difference between the discounted future occupancy of the target state under the action-dependent SRs (eq. 2) corresponding to the "smaller" (left) and "greater" (right) actions. The x -axis denotes the states, and the y -axis denotes the difference between the SRs.

C Generalisation to non-spatial task

In the main paper we argued that the same set of eigenvectors can be used to predict future occupancy distribution given the transition matrix for symmetrical relations like diffusion between adjacent states and directed transitions (e.g. moving N S E W). Here we briefly discuss the generalisation of our model to non-spatial tasks.

We could apply our method to the one-dimensional transitive inference tasks of this type. e.g., given $A > B, B > C, C > D$, then infer if $A > D$ [34]? This would be like having a 1D track (and Fourier eigenvectors for 1-step transitions in both directions) corresponding to actions "greater" or "smaller", and using "intuitive planning" to see if using eigenvalues for "greater" will take you from A to B in the discounted future more likely than eigenvalues for "smaller". In order to deal with the non-periodicity of the task, we simulate transitive inference in a small subset of the state space of the torus. As shown in Fig. 11, we see that our framework correctly predicts the transitive relationship between the chosen state x_{129} and states close to x_{129} .

Despite the simplicity of 1D transitive inference (Fig. 11), our model is still an advance on the original intuitive planning method which was restricted to symmetric transition structures, and so indicates distance but not direction.

D Simulation details

All simulations were implemented in Python. The simulation details for each task is as follows:

- Fig. 1: $\mathbb{P}(s_{t+1} = i + 1 | s_t = i) = \mathbb{P}(s_{t+1} = i - 1 | s_t = i) = 0.5$, $\gamma = 0.9$ for generating the resolvent measure (eq. 2).
- Fig. 2: Variance of each Gaussian field is 3; **B**: $(0, 5)$ drift velocity with increasing diffusion (variance increase by 3 per step); **C**: plain $(3, 3)$ drift velocity; **E**: $\gamma = 0.9$.
- Fig. 3: Variance of each Gaussian field is 1.5, $\gamma = 0.9$; **C**: ϵ -greedy: $\epsilon = 0.05$.
- Fig. 4: Variance of each Gaussian field is 2, $\gamma = 0.9$, $\lambda = 2$ (eq. 32).
- Fig. 5: **A**: wavevectors of chosen input Fourier modes: $\mathbf{k}_1 = (4/50, 1/50)$, $\mathbf{k}_2 = (1/50, 4/50)$, $\mathbf{k}_3 = (3/50, -3/50)$, $\mathbf{k}_4 = (-4/50, -1/50)$, $\mathbf{k}_5 = (-1/50, -4/50)$, $\mathbf{k}_6 = (-3/50, 3/50)$; **B**: real rat trajectory projected onto 50×50 2D spatial domain, firing phase interval: $[-\pi/4, \pi/4]$ of the phases of the Fourier modes, within which the Fourier modes fire spikes, integration time interval: $p_{int} = 12$, exponential decay rate: $\eta = 0.2$, where the exponential decay windy is $\{\exp(-\frac{p_{int}-i}{\eta p_{int}})$ for $i = 0, \dots, p_{int} - 1\}$, grid cell firing threshold: 2.95, directional bias: within $\pm\pi/2$ of the head direction (the range of the relative difference between the direction of the wavevector and the head direction, within which the Fourier modes are allowed to fire); **C**: running direction: $\arctan(1/3)$, the firing phase of the simulated grid cell is computed by assuming each timestep is a cycle.
- Fig. 9: $\gamma = 0.9$, $\lambda = 2$ (eq. 32);
- Fig. 11: $\gamma = 0.3$, number of states: 260, number of effective transitive inference states: 87.

We will submit codes for reproducibility with the accepted paper.